

# Effect of Specimen Thickness on Microstructural Changes During Oxidation of the NiCrW Alloy 230 at 950–1050°C

A. JALOWICKA,<sup>1,3</sup> R. DUAN,<sup>1</sup> P. HUCZKOWSKI,<sup>1</sup> A. CHYRKIN,<sup>1</sup>  
D. GRÜNER,<sup>1</sup> B.A. PINT,<sup>2</sup> K.A. UNOCIC,<sup>2</sup> and W.J. QUADAKKERS<sup>1</sup>

1.—Institute for Energy and Climate Research, IEK-2, Forschungszentrum Jülich GmbH, 52425 Jülich, Germany. 2.—Materials Science & Technology Division, Oak Ridge National Laboratory, Oak Ridge, TN 37831, USA. 3.—e-mail: a.jalowicka@fz-juelich.de

An accurate procedure for predicting oxidation-induced damage and lifetime limits is crucial for the reliable operation of high-temperature metallic components in practical applications. In order to develop a predictive oxidation lifetime model for Ni–Cr alloys, specimens of wrought NiCrW alloy 230 with different thicknesses were cyclically oxidized in air at 950–1050°C for up to 3000 h. After prolonged exposure, two types of carbides as well as a Cr-rich nitride ( $\pi$ -phase) precipitated in the  $\gamma$ -Ni matrix. The oxidation-induced loss of Cr from the alloy resulted in the formation of subscale zones, which were free of the Cr-rich carbide and nitride but also of the Ni–W rich  $M_6C$ . The width of the  $M_6C$ -free zone was smaller than that free of the Cr-rich precipitates. Thermodynamic and diffusion calculations of the observed time- and temperature-dependent Cr depletion processes identified that back diffusion of C occurred which resulted in an increased volume fraction of  $M_{23}C_6$  in the specimen core. With increasing time and temperature, the amount of  $\pi$ -phase in the specimen core increased. The subscale depletion of the initially present Cr-nitrides and the formation of Cr-nitrides in the specimen center is believed to be related to a mechanism which is qualitatively similar to that described for the Cr carbide enrichment. However, with increasing time and decreasing specimen thickness, N uptake from the atmosphere becomes apparent. As a result, the precipitates present in the specimen center eventually consisted almost exclusively of nitrides.

## INTRODUCTION

Most high-temperature wrought Ni-based alloys rely for protection against oxidation attack on the formation of a slowly growing, adherent chromia-base surface oxide or scale, which forms due to the selective oxidation of Cr.<sup>1</sup> The most common wrought alloys have no or minimal amounts of  $\gamma'$  and rely on solid solution strengthening by Cr, Mo, Co and W<sup>2,3</sup> as well as carbide precipitates (e.g., of the type  $M_{23}C_6$  or  $M_6C$ ) for creep strength.<sup>4,5</sup> Especially at lower temperatures (e.g., 700°C), intermetallic phases also may contribute to the creep strength of the alloy.<sup>6</sup> However, long-term aging at lower temperatures may result in excessive formation of intermetallic and carbide precipitates, which may adversely affect material ductility.<sup>6–8</sup>

Especially when oxidized at high temperatures ( $\geq 900^\circ\text{C}$ ), the oxidation resistance of wrought Ni-base alloys will gradually deteriorate due to the preferential removal of Cr from the alloy due to Cr consumption by oxide scale growth and re-growth if the scale spalls. The Cr depletion eventually results in a decrease of the Cr concentration at the alloy-oxide interface to such a low level that the growth of the protective chromia scale can no longer be sustained. This leads to the formation of rapidly growing, less protective oxide phases such as NiO and/or  $\text{NiCr}_2\text{O}_4$  and is frequently termed “break-away oxidation”.<sup>9</sup>

Before breakaway occurs, the oxidation-induced Cr depletion may also affect material properties (e.g., creep strength, ductility) due to changes in the alloy microstructure,<sup>10–12</sup> i.e. the amount and

distribution of strengthening precipitates. Obviously, these depletion-induced processes will be more significant in thin-walled components. A commonly encountered example is the subsurface dissolution of Cr-rich carbides,<sup>13–18</sup> and the effect of a carbide-free subscale zone on alloy mechanical properties has been previously discussed.<sup>8</sup> Thus, to predict component performance in long-term applications, the model must quantify Cr depletion as a function of time and temperature but also its effect on the microstructure.

The present investigation on alloy 230 was part of a larger project to model the lifetime of thin-walled NiCr components. Alloy 230 is a commonly used high-temperature alloy for combustor liners, honeycomb structures and heat exchangers.<sup>19</sup> This paper focuses on the microstructural changes as a function of specimen thickness, oxidation time and temperature. Additional results and more theoretical considerations related to oxidation-induced lifetime limits will be presented elsewhere.<sup>20</sup>

## EXPERIMENTAL

The alloy 230 specimens were all fabricated from a 1.2-mm-thick sheet in the solution-annealed condition, supplied by Haynes International. Bulk chemical analyses were performed by inductively coupled plasma–optical emission spectroscopy (ICP–OES) after completely dissolving the metal in aqua regia. The concentrations of C, N, S and O were determined using combustion–infrared analysis. Table I shows that the composition was very close to the nominal values; however, the Co and Fe contents were much lower than the maximum values and the La content was not detected by the ICP–OES process. Specimens of  $20 \times 10 \text{ mm}^2$  were ground to nominal thicknesses of 0.2 mm, 0.3 mm and 0.5 mm and then polished to a P1200 surface finish. Prior to oxidation, the specimens were degreased in ethanol. Oxidation exposures at 950°C, 1000°C and 1050°C in laboratory air were conducted for 1000 h or 3000 h. For the 1000°C and 1050°C experiments at Forschungszentrum Jülich, the specimens were exposed in 50-h cycles and hung on alumina rods in alumina crucibles, which enabled the determination of the specimen mass change, amount of spalled oxide and the total mass gain (i.e. specimen + spalled oxide, in the following termed as “total mass gain”). At 950°C, the specimens were exposed in 10-h cycles with 10 min cooling between

cycles and weighed once per week at 16-cycle intervals at Oak Ridge National Laboratory. In the automated vertical cyclic rig, the specimens were held on alumina rods with a Pt-10Rh wire and only the specimen mass changes were determined.<sup>21</sup>

After oxidation, the specimens were sputtered with a thin gold layer followed by Ni plating in a NiSO<sub>4</sub> bath before standard metallographic cross-section preparation. Sectioned specimens were then analyzed using light optical microscopy, scanning electron microscopy (SEM), energy dispersive x-ray spectroscopy (EDX) using a field emission gun SEM (Zeiss Supra 50VP) and electron backscatter diffraction (EBSD; Zeiss Merlin). Selected specimens were analyzed by glow discharge optical emission spectroscopy (GDOES) whereby quantification procedures described in references<sup>22,23</sup> were used.

Thermodynamic calculations of the phase equilibria were carried out with the software package Thermo-Calc v.5 using the database TTN17. The volume fraction of precipitates as well as the depth of the precipitate-free zone was calculated using the computer software AnalySIS pro 5.0.

## RESULTS

Figure 1 shows an example of the mass change data at 1000°C in laboratory air illustrating the typical effect of specimen thickness on oxidation kinetics. The oxidation kinetics at other temperatures showed similar trends and are presented elsewhere.<sup>20</sup> The mass change at 1000°C was independent of specimen thickness until  $\sim 400$  h of exposure (Fig. 1). After longer exposure times, the specimen and total mass changes for the 0.3- and 0.5-mm specimens began to deviate, indicating scale spallation. The total mass gains for both specimens remained similar, but the extent of scale spallation was slightly more pronounced for the thicker specimen.

For the 0.2-mm-thick specimen, there was only a minor difference between the specimen and total mass gains indicating that little or no scale spallation occurred up to 3000 h. However, after  $\sim 500$  h, the total mass gain deviated from near-parabolic behavior to almost linear kinetics.

Figure 2 shows Cr profiles measured by EDX for specimens of different thickness after 1000 h and 3000 h exposure at 1000°C. It should be noted that

**Table I. Chemical composition (in wt.%) of the studied alloy 230 heat determined by ICP–OES and combustion infrared analysis compared with nominal composition supplied by the manufacturing data sheet<sup>24</sup>**

	Cr	W	Mo	Fe	Mn	Si	Al	Co	La	C	N	O	S
Nominal	22.0	14.0	2.0	3.0 (max.)	0.5	0.4	0.3	5.0 (max.)	0.02	0.10	–	–	–
Analyzed	22.2	14.3	1.28	1.23	0.49	0.41	0.37	0.14	<0.01	0.092	0.060	0.002	<0.01

the EDX point analyses measured the Cr concentration in the alloy matrix and do not take into account the Cr tied up in the precipitate phases which possesses a size that is clearly visible in the SEM image. After 1000 h, a subscale Cr depletion was apparent and the Cr mass fraction at the scale–alloy interface for all of the specimens shown in Fig. 2a was ~17%. After 3000 h (Fig. 2b), the Cr concentrations at the scale–alloy interface for the thicker specimens were quite similar, i.e. ~15%. However, for the 0.2-mm specimen, the depletion profile reached the center of the sample. With a

severely depleted Cr reservoir, the result was a substantial decrease in the Cr interface concentration, as expected from theoretical considerations.<sup>25</sup>

In order to obtain information about the alloy microstructure without it being affected by the subscale depletion process, a 0.5-mm specimen was isothermally exposed at 1000°C for only 100 h. Figure 3 shows that the alloy exhibited a four-phase microstructure consisting of a face-centred cubic  $\gamma$ -Ni matrix and three types of precipitates. EDX revealed one of the precipitates (black arrows) to be rich in W and Ni, likely  $M_6C$ ,<sup>6,26</sup> whereas the other type of precipitate (white arrows) was a Cr-rich nitride with typical composition with respect to metallic constituents in atomic percent: 37Cr-34Ni-15W-4Mo-10Si. Only traces of a Cr-rich carbide (black dashed arrows), probably  $M_{23}C_6$ <sup>27</sup> were found, mainly at alloy grain boundaries. These precipitates were too small for quantitative analysis by EDX at this stage.

The typical microstructural features of alloy 230 specimens after prolonged oxidation is shown in Fig. 4, using the 0.3-mm specimen after 3000 h exposure at 1000°C as an example. Apart from the internal aluminum oxide, three types of precipitates were observed in the alloy (in the BSE image appearing white and gray, respectively). These precipitates were absent beneath the scale and were mainly present in the center of the specimen. Comparing Figs. 3 and 4, the volume fraction of precipitates appeared to increase with increasing exposure time.

The precipitates formed after prolonged exposure could be unequivocally identified by EDX and EBSD (Fig. 5). Figure 5a shows a BSE image from the center of the 0.3-mm specimen oxidized at 1000°C for 3000 h, and Fig. 5b–g are element maps from

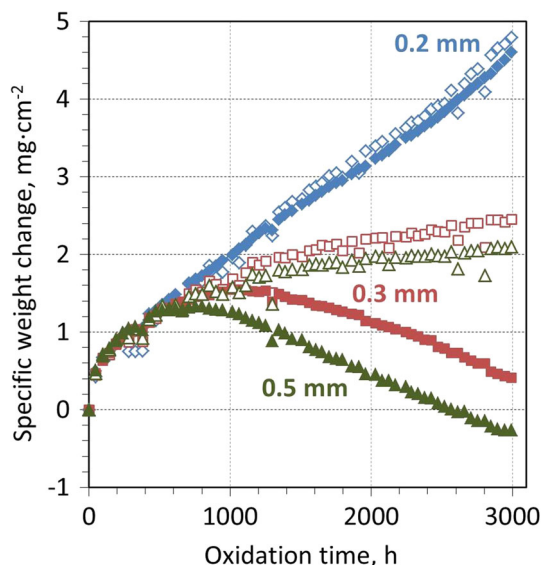


Fig. 1. Typical example of mass change of alloy 230 (with specified specimen thicknesses) during oxidation in laboratory air at 1000°C. The open and closed symbols indicate the total and specimen mass changes, respectively.

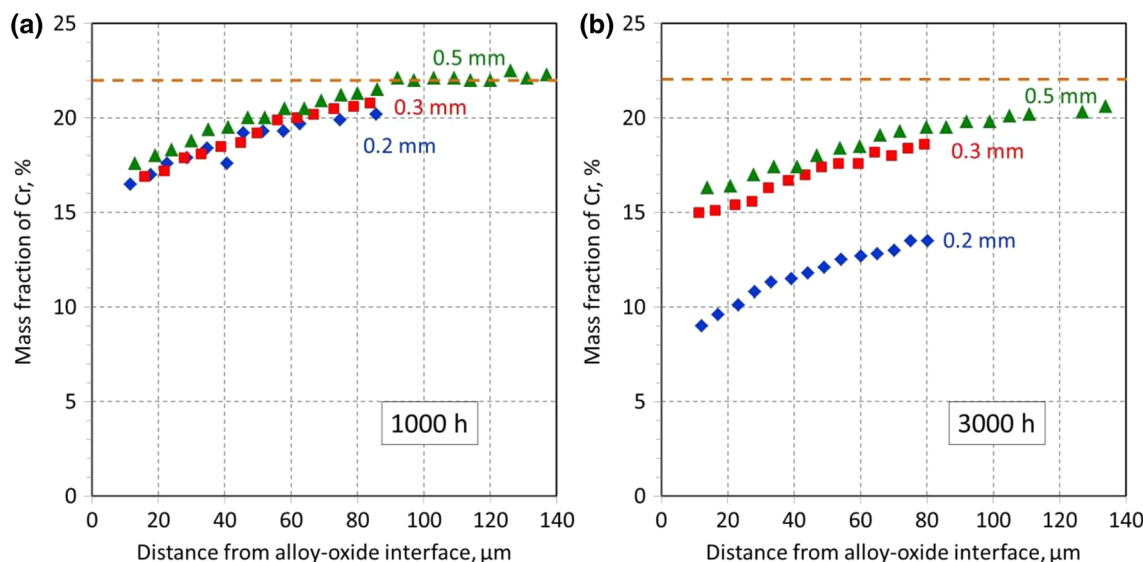


Fig. 2. Cr profiles measured by EDX (measured in  $\gamma$ -Ni matrix) for specimens of different thicknesses after (a) 1000 h and (b) 3000 h exposure at 1000°C (Dashed line the original Cr concentration in alloy 230).



this region. The carbide appearing bright in the BSE image is rich in Ni and W (similar to Figs. 3 and 4) with some Mo present, whereas the other carbide is Cr-rich.

The result of the EBSD phase map for the same specimen is shown in Fig. 6a, confirming the presence of  $M_{23}C_6$  and  $M_6C$  phases after long-term oxidation at 1000°C. EDX analyses indicated typical compositions of the metallic constituents in the two carbide precipitates (in wt.%) to be 63W-20Ni-12Cr-5Mo for  $M_6C$  and 40Cr-32Ni-24W-4Mo for  $M_{23}C_6$ .

Additionally, nitride precipitates could be identified (Figs. 5c and 6b) which were isostructural with  $Ni_2W_3N$  ( $\pi$ -phase)<sup>28,29</sup> with typical concentrations of the metallic constituents (in wt.%) 39Cr-32Ni-24W-4Mo. Unlike the nitride phase observed in the specimen exposed for only 100 h (Fig. 3), no Si was found in the  $\pi$ -phase precipitates. In some

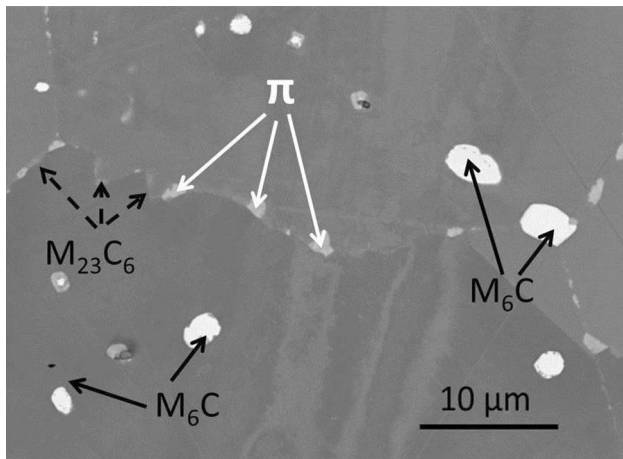


Fig. 3. BSE image of bulk alloy 230 (0.5 mm thick sample) showing microstructure after 100 h isothermal exposure in synthetic air at 1000°C (Black, black dashed and white arrows W-rich carbides, Cr-rich carbides and Cr-rich nitrides (indicated as  $\pi$ ) respectively).

specimens and/or specimen areas, the Cr-rich carbides and nitrides coexisted (Fig. 5a) whereas in some places only carbides or nitrides were present.

The microstructural evolution of alloy 230 as a function of time and specimen thickness at 1000°C is shown in Fig. 7. Only one temperature was chosen for the illustration because the trends were found to be qualitatively similar for all three temperatures. In all cases, the scale was predominantly  $Cr_2O_3$  with minor amounts of alumina internal oxidation, which preferentially nucleated along alloy grain boundaries. This morphology is very common for commercial Ni-Cr alloys with high (>20%) Cr contents and low Al contents.<sup>30</sup> (The Al may be intentional or an impurity associated with commercial alloy manufacturing.) On top of the chromia layer, a very thin Mn-rich oxide, likely  $MnCr_2O_4$ , was found to be present. However, due to the very limited Mn reservoir in the specimens, no unequivocal indications for spinel formation were found after longer exposures, especially in the thinnest specimens. The scale thickness varied from 6  $\mu m$  to 30  $\mu m$ . The scale on the 0.2-mm specimens was substantially thicker than that on the 0.3- and 0.5-mm specimens, in agreement with the gravimetric data (Fig. 1). Additionally, minor void formation was found in the subsurface zone, probably related to the Kirkendall effect.<sup>1</sup> Figures 4 and 7 clearly show that the width of the region, which was free of Cr-rich carbide and nitride precipitates (blue dashed lines), is slightly wider than that of the  $M_6C$  depletion zone (red dashed line). For the 0.2-mm specimen, almost all the  $M_6C$  precipitates were consumed after 3000 h at 1000°C (Fig. 7f).

Table II summarizes the measured volume fractions, expressed as a percentage, of  $M_6C$  and the Cr-rich precipitates at 1000 h and 3000 h for the three specimen thicknesses. Particularly for the thin specimens, the quantitative estimation of the volume fractions of the various precipitates in the specimen center was difficult, due to the limited width of the precipitate-containing zone. Also, in the

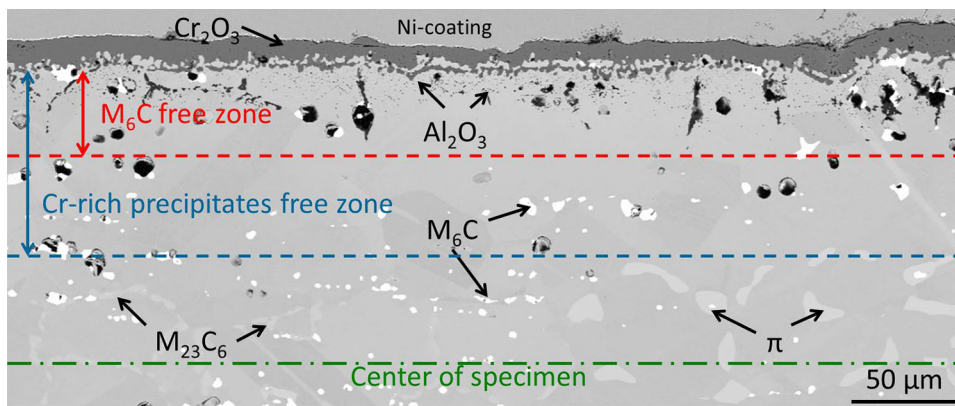


Fig. 4. BSE image of 0.3-mm-thick alloy 230 after reaction for 3000 h in laboratory air at 1000°C. Designations of phases are based on EDX and EBSD results in Figs. 5 and 6. Labeled precipitates in the lower part are Ni/W-rich  $M_6C$  carbides, Cr-rich  $M_{23}C_6$  carbides and Cr-rich nitrides (indicated as  $\pi$ ).

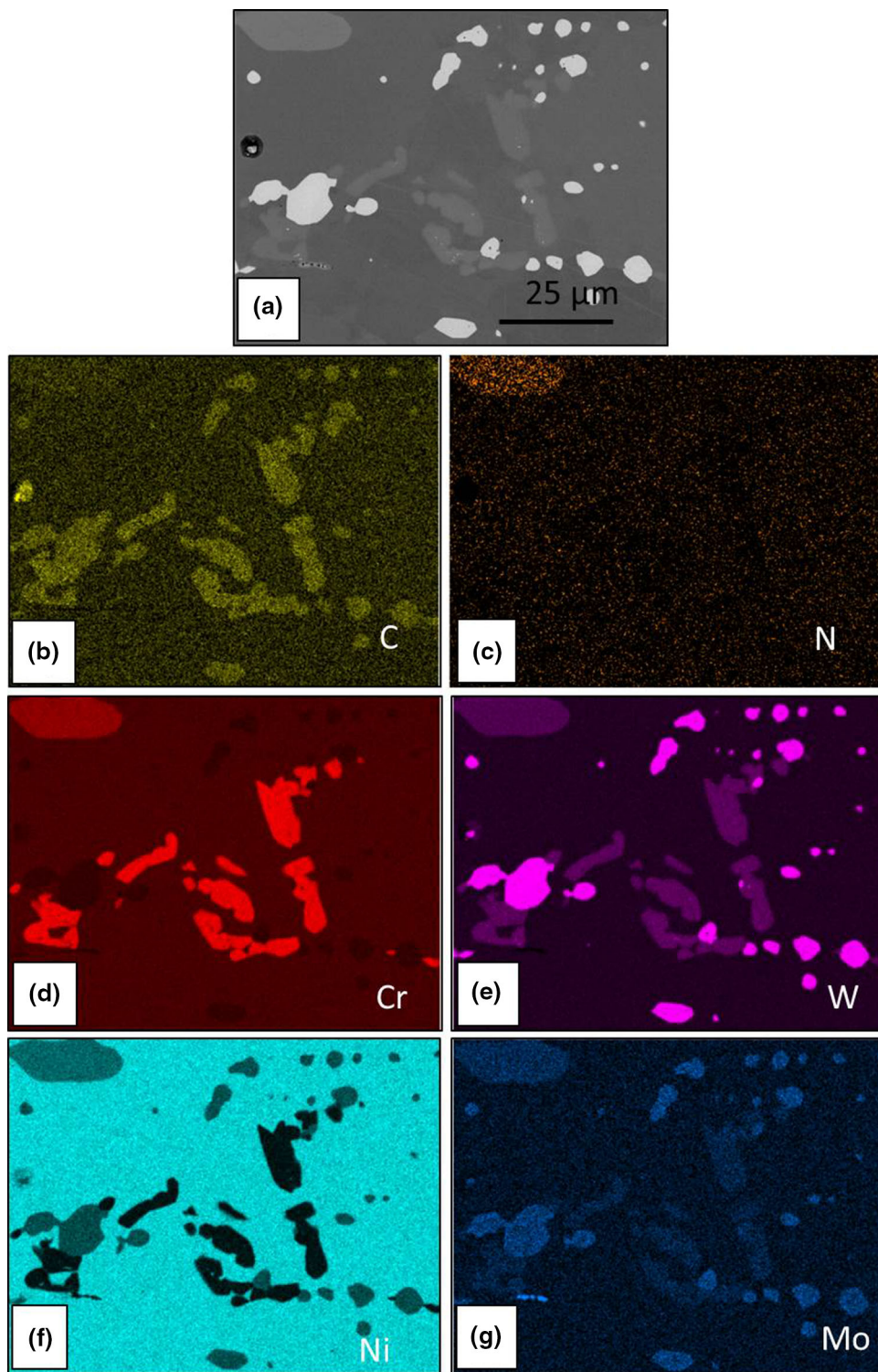


Fig. 5. (a) BSE image with (b–g) EDX element maps from the center of a 0.3-mm-thick alloy 230 specimen oxidized for 3000 h at 1000°C in laboratory air. The location used for the measurement corresponds to the left side of Fig. 4).

BSE images, it was difficult to distinguish between the two types of Cr-rich precipitates ( $M_{23}C_6$  and Cr-nitrides) in the AnalySIS pro 5.0 software due to the similarity in contrast. Thus, these precipitates were summed in Table II. In spite of the quantification difficulties, the results show that the volume

fraction of Cr-rich precipitates in the center of the specimen increased with exposure time and the volume fraction of  $M_6C$  tended to decrease. This was also found at the other temperatures as will be discussed later in the present section. As illustrated in Figs. 5 and 6, Cr-rich  $M_{23}C_6$  and  $\pi$ -phase co-



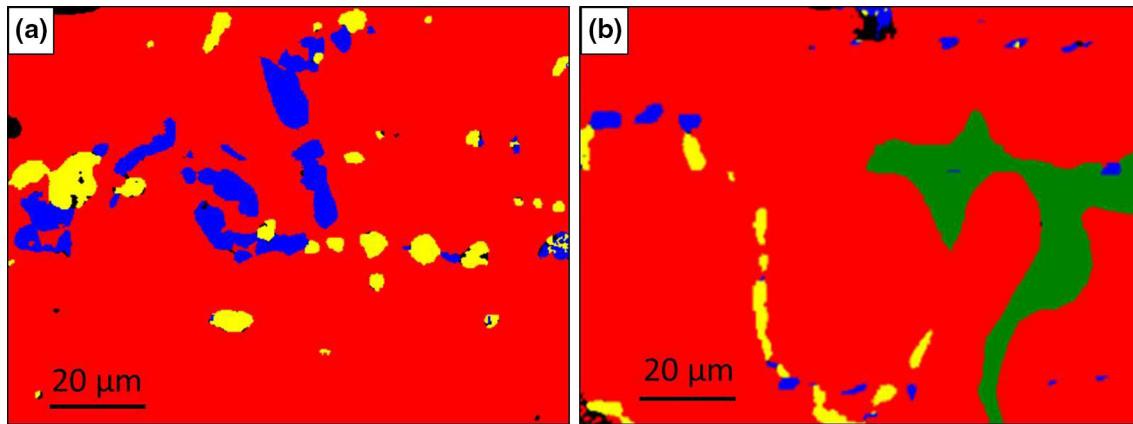


Fig. 6. EBSD phase map for alloy 230 in two different places (a, b) in the center of the 0.3-mm specimen after 3000 h oxidation at 1000°C in laboratory air. In the EBSD phase map red corresponds to the  $\gamma$ -Ni matrix, yellow to  $M_{23}C_6$ , blue to  $M_6C$  and green to  $\pi$ - $Ni_2W_3N$ . The location used for the measurement in (a) corresponds to the left side of Fig. 4; the location used for the measurement in (b) corresponds to the right side of Fig. 4.

existed in the core of some specimens. However, there was a clear trend that with increasing exposure time and decreasing specimen thickness the relative amount of nitride increased at the expense of  $M_{23}C_6$ , until in the thinnest specimen after 3000 h the Cr-rich precipitates consisted solely of nitrides (Fig. 7f).

The width of the  $M_6C$ -free subsurface zone in the 0.5- and 0.3-mm-thick specimens was smaller than that of the zone free of Cr-rich precipitates (Fig. 7a–e). In the 0.2-mm specimen, a similar trend was observed in the specimen oxidized for 1000 h (Fig. 7c). However, the area in which Cr-rich precipitates (here  $\pi$ -phase) were present after 3000 h was limited to a narrow zone of approximately 50  $\mu m$  around the center of the specimen. Hardly any precipitates of the  $M_6C$  were found (Fig. 7f).

Table III summarizes the widths of the carbide/nitride free subsurface zones after the 1000°C exposures shown in Fig. 7. The data illustrate that the widths of the zones which were free of Cr-rich precipitates increased with increasing exposure time and specimen thickness. An exception is the thickest specimen in which the Cr-rich precipitate-free zone after shorter exposure time was larger than after 3000 h. That, however, may be caused by the fact that the Cr-rich precipitates in the specimen oxidized for 1000 h were very small and that the measurements might be subject to a larger error.

To illustrate the effect of temperature, Fig. 8 shows the microstructures of 0.2-mm-thick alloy 230 specimens oxidized for 3000 h at 950°C and 1050°C. At both temperatures, a subscale region free of carbide and nitride precipitates developed as a result of Cr consumption by oxide scale formation, like at 1000°C. However, the widths of these precipitate-free zones were much less pronounced at the lowest oxidation temperature. The enrichment of the Cr-rich precipitates in the specimen center at 950°C (Fig. 8a) was, as expected, far less significant

than that observed after exposure at 1000°C (Fig. 7f) and at 1050°C (Fig. 8b). (Note that the 1050°C specimen was stopped after 2000 h due to breakaway oxidation at the specimen corners.<sup>20</sup>)

Both the 0.2- and 0.5-mm-thick specimens exposed at 950°C contain  $M_6C$  and Cr-rich precipitate phases (Fig. 9). The images in Fig. 9 indicate that the volume fraction of the Cr-rich precipitates near the specimen center increased with increasing oxidation time (compare Fig. 9a with b, and c with d) and decreasing specimen thickness (compare Fig. 9a with c, and b with d) as was observed for the specimens oxidized at 1000°C. It is interesting to note that, for the 0.2-mm specimens after 1000 h and 3000 h as well as for the 0.5-mm specimen after 3000 h,  $M_6C$  as well as Cr-rich carbide and nitride were found. However, for the 0.5-mm specimen after 1000 h, no indications of the presence of Cr-rich carbides could be detected.

At 1050°C, the dissolution of the  $M_6C$  carbides in the subscale region was similar to the observations at 1000°C. A subsurface zone depleted in carbide and nitride was clearly apparent after the 1000 h exposure (Fig. 10). The Cr-rich precipitates in the center after 3000 h exposure mainly consisted of nitride. There was a tendency that some  $M_6C$  precipitates appeared again after 3000 h (Fig. 10) in the subsurface zone. A similar observation was made for the 0.3-mm specimen. For the 0.2-mm specimen after 2000 h, only a very narrow Cr-nitride layer was present in the specimen center, showing similar features as after 3000 h at 1000°C (Figs. 7f and 8b).

## DISCUSSION

### Oxidation Kinetics

In interpreting the mass change data (Fig. 1), it has to be borne in mind that oxidation of chromia-forming alloys in high  $pO_2$  gases (such as air) will be

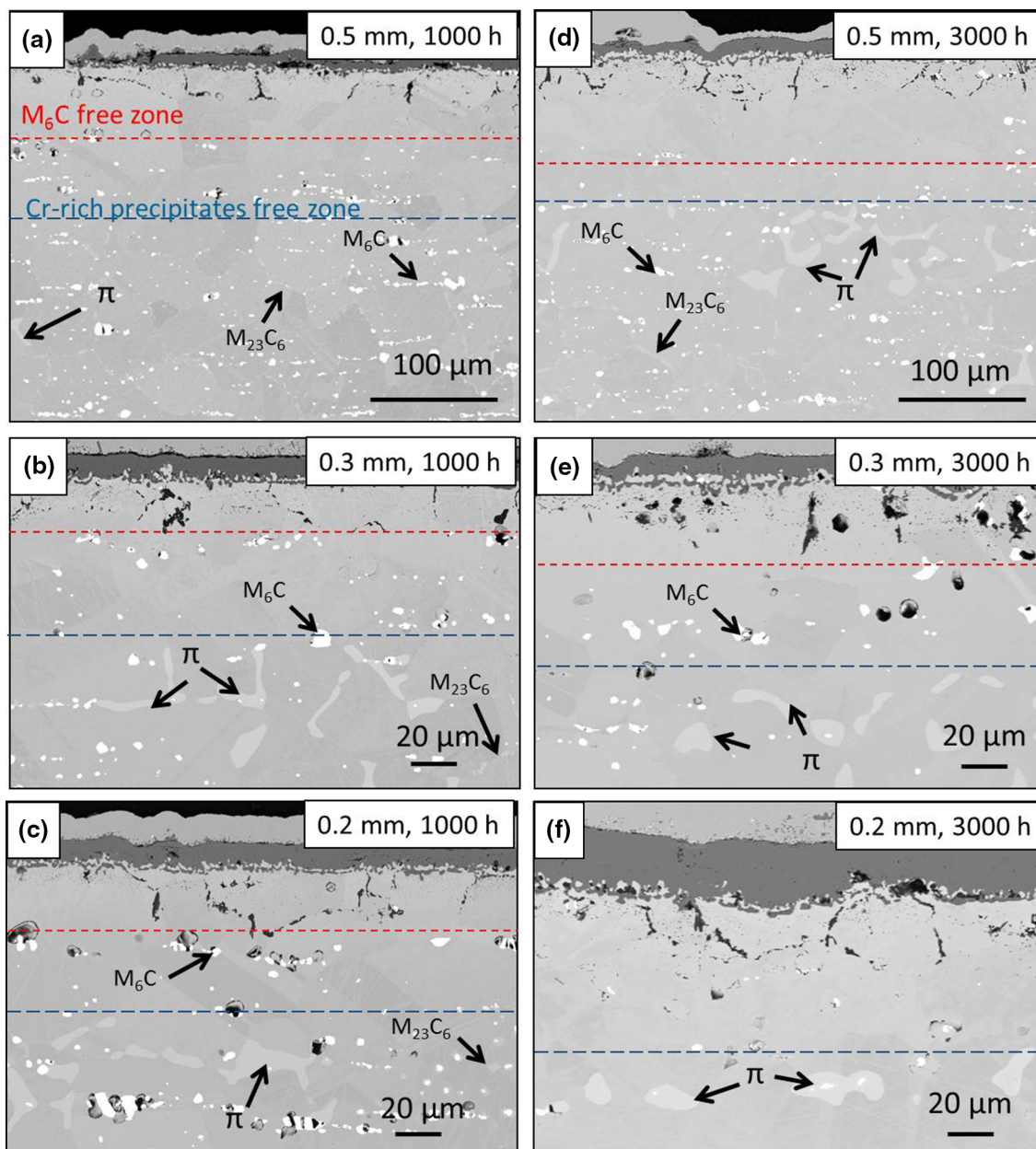


Fig. 7. BSE images of (a, d) 0.5 mm, (b, e) 0.3 mm and (c, f) 0.2-mm-thick alloy 230 after reaction for (a–c) 1000 h and (d–f) 3000 h in laboratory air at 1000°C (blue and red dashed lines indicate the width of the zones depleted in  $M_6C$  and Cr-rich precipitates, respectively)..

affected by the formation of volatile Cr species, such as  $CrO_3$  and  $CrO_2(OH)_2$  in the presence of  $H_2O$ .<sup>31–33</sup> Based on relevant data,<sup>34</sup> the mass loss induced by this effect in static laboratory air in the temperature range considered would be in the range of a few tenths of a  $mg/cm^{-2}$  for a pure chromia scale up to the maximum exposure time and thus should not fundamentally alter the mass change kinetics in the present study. It also should be mentioned that the Mn in alloy 230 (Table I) is known to form a thin outer layer of  $(Cr, Mn)_3O_4$  on top of the chromia scale.<sup>35</sup> This spinel layer has been shown<sup>36</sup> to reduce the formation of volatile Cr species. Thus, formation of volatile Cr species certainly occurs, but

it is not expected to substantially affect the measured kinetics and related subscale depletion phenomena.

The results in Fig. 1 show, as expected, increasing oxidation rates with increasing temperature. Considering the O/Cr mass ratio and the well-known density of chromia ( $5.2 g cm^{-3}$ ),<sup>37</sup> it is easy to derive that, for growth of a pure chromia scale, an area-specific O uptake of  $1 mg cm^{-2}$  corresponds to a scale thickness of  $6.07 \mu m$ . Ignoring the very minor amounts of spinel phase and the O uptake by internal oxidation, the scale thicknesses derived from weight gains may be compared with the actually prevailing scale thicknesses visible in the

**Table II. Volume fraction (%) of respective precipitates in the specimen center after oxidation at 1000°C (see text for detailed explanation)**

Specimen thickness (mm)	Exposure time (h)			
	M <sub>6</sub> C		Cr-rich precipitates	
	1000	3000	1000	3000
0.2	22	13	5	6
0.3	15	9	4	9
0.5	10	8	2	12

**Table III. Depth of the subsurface zones ( $\mu\text{m}$ ) which were free of M<sub>6</sub>C and Cr-rich precipitates (carbides and nitrides) in specimens oxidized at 1000°C**

Specimen thickness (mm)	Exposure time (h)			
	M <sub>6</sub> C		Cr-rich precipitates	
	1000	3000	1000	3000
0.2	41	67	77	90
0.3	49	79	96	121
0.5	74	91	134	126

metallographic cross sections (Fig. 7). As an example: the 0.2-mm specimen exhibited a mass gain of  $1.95 \text{ mg cm}^{-2}$  after 1000 h at 1000°C, which would correspond to a scale thickness of  $11.8 \mu\text{m}$ . This is in good agreement with the value seen in the metallographic cross-section (Fig. 7c). It is easy to verify that, in spite of the mentioned sources of inaccuracy, in all cases very reasonable agreement between calculated and measured values prevails.

For all studied temperatures, oxide adherence was found to increase with decreasing specimen thickness. This is in qualitative agreement with previous results and theoretical considerations related to the effect of specimen thickness on oxide scale adherence.<sup>38</sup> Whereas no indication for oxide spallation for the 0.2-mm specimens was found, the 0.3- and 0.5-mm specimens exhibited the onset of scale spallation after approximately 300 h at 1050°C, 600 h at 1000°C (Fig. 1) and 2000 h at 950°C. At the times at which the thicker specimens started to exhibit scale spallation, the 0.2-mm specimen showed oxidation kinetics which were faster than parabolic. This enhanced oxidation might be related to relaxation of growth stresses by plastic deformation of the metallic substrate,<sup>39,40</sup> rapid exhaustion of the reservoir of the reactive

element La<sup>39,41</sup> or, more likely, to tensile microcracking occurring upon re-heating after repeated specimen cooling, as described elsewhere.<sup>38,42</sup>

### Modelling M<sub>6</sub>C Dissolution and M<sub>23</sub>C<sub>6</sub> Formation

It is well established that long-term, high-temperature exposure of Ni base alloys generally results in precipitate coarsening.<sup>43</sup> In the present case, however, the precipitate size and morphology were mainly affected by subscale changes in alloy composition, especially due to the Cr depletion for these relatively thin specimens oxidized at high temperature. The experimental results show that the Cr depletion leads to formation of precipitate-free subscale zones, and that the widths of these zones for the various precipitate types (carbides and nitrides) differ substantially. Also, the volume fraction of Cr-rich precipitates (M<sub>23</sub>C<sub>6</sub> and Cr-nitrides) in the specimen center increased with time. In most samples, the amount of M<sub>23</sub>C<sub>6</sub> was larger after 1000 h than after 3000 h, where mainly nitrides were found. These effects increased with temperature and decreasing specimen thickness. At the extreme of the 0.2-mm-thick specimen after 3000 h at 1000°C and 2000 h at 1050°C, the M<sub>6</sub>C carbide tended to vanish completely.

Thermodynamic calculations revealed that, for the C content (i.e. 0.09%) prevailing in the as-received alloy 230, only  $\gamma$ -Ni and M<sub>6</sub>C exist in addition to a very minor amount of Cr-rich nitride. Based on the experimental findings (Fig. 6), it was assumed in the calculations that the  $\pi$ -phase was the only Cr-rich nitride which may be formed. If the C content was increased to  $\sim 0.16\%$ , the calculation then predicted M<sub>23</sub>C<sub>6</sub> formation with a corresponding decrease in M<sub>6</sub>C fraction as the C content further increased (Fig. 11). As the major precipitate phase in the as-received material is M<sub>6</sub>C carbide, the first part of the discussion focuses on the carbides and initially ignores the nitrides.

To assist in understanding the mechanism of the observed microstructural changes in alloy 230 during oxidation, a section of the Ni-Cr-W-Mo-C phase diagram at 1000°C was calculated with fixed 14 wt.% W and 2 wt.% Mo. The trends discussed for 1000°C are qualitatively similar for the range of temperatures studied. The phase diagram together with C isoactivity lines are shown in Fig. 12. (An isoactivity line is a locus of compositions in the phase diagram for which the chemical potential (i.e. activity) of the selected element (C) is constant.) Point A in Fig. 12 indicates that the bulk composition of alloy 230 is located in a two-phase field in which the Ni-matrix is in equilibrium with the W-rich M<sub>6</sub>C carbide, as shown in Fig. 11.

During high-temperature oxidation, the Cr concentration at the scale-alloy interface decreases due to the continuous Cr depletion related to the scaling process (Fig. 2). Moving from point A to point P in



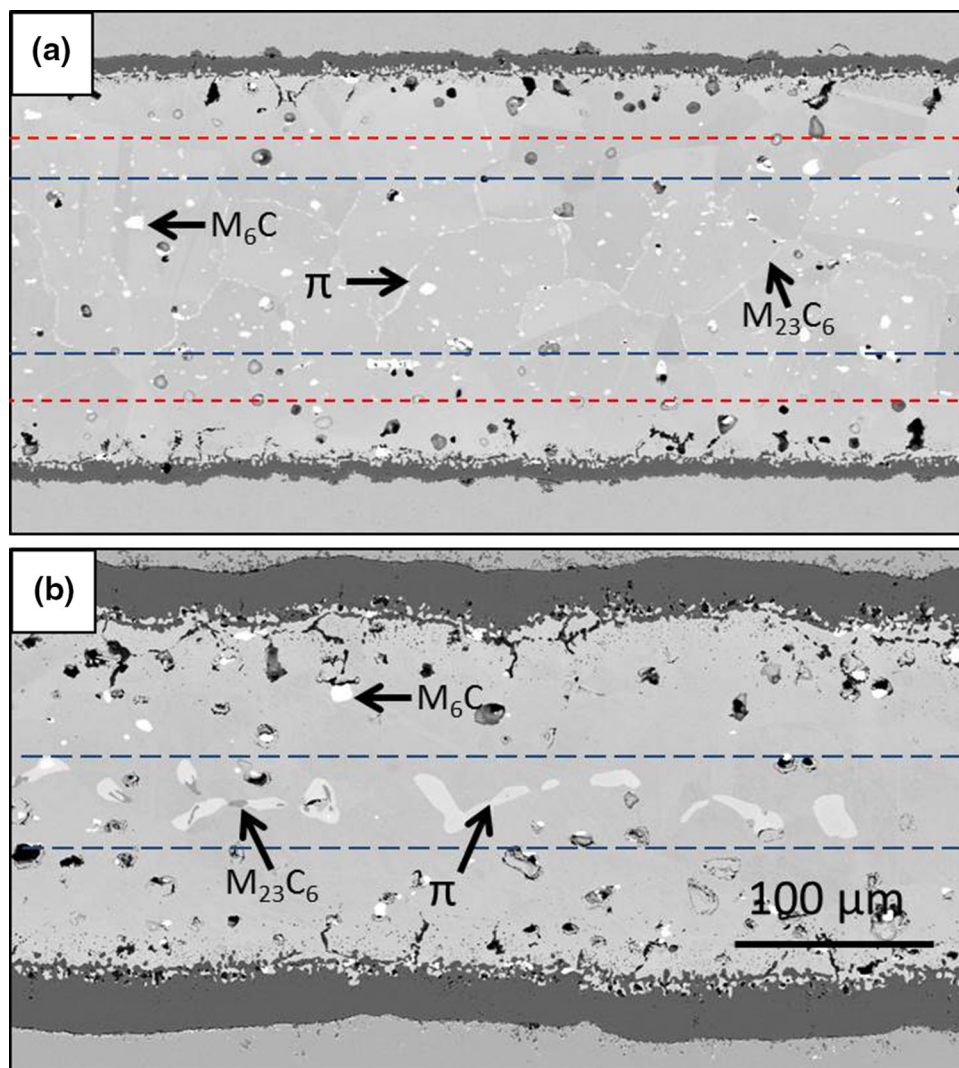


Fig. 8. BSE images for 0.2-mm-thick alloy 230 specimens after reaction for (a) 3000 h at 950°C h and (b) 2000 h at 1050°C in laboratory air (blue and red dashed lines indicate the width of the zones free of  $M_6C$  and Cr-rich precipitates, respectively).

Fig. 12, as the Cr content decreases, results in an increase in the solubility of the  $M_6C$  carbide. This may at first sight be surprising as the carbide mainly contains Ni, W and some Mo, but hardly any Cr. The reason for this dependence of  $M_6C$  solubility on Cr content is related to the thermodynamic interactions of the alloying elements in the  $\gamma$ -Ni matrix, specifically, the effect of Cr content on the activity of C and W. The thermodynamic calculations in Fig. 13 show that the W activity decreases with decreasing Cr content, thus destabilizing the  $M_6C$  carbide. The effect of Cr on the thermal stability of  $M_6C$  in a Ni-base alloy has been extensively discussed.<sup>44</sup> Figure 13 also shows that Cr depletion leads to an increased C activity. The Cr-depleted near-surface region of the alloy is thus an area of high C activity compared to that in the middle of the specimen. The resulting C activity gradient creates a driving force for C to diffuse from the Cr-depleted surface region to the specimen center in order to

maintain equilibrium. In Fig. 12, this means that the diffusion path for this transformation will be close to the isoactivity line from point A to point B.

Back diffusion of C as a result of oxidation-induced Cr-depletion has been described in previous studies, e.g., for the Ni-base alloy 617.<sup>7,16,45–47</sup> The back diffusion has generally been explained to be the result of the Cr-depletion-induced dissolution of the Cr-rich carbide. The dissolution of the carbide obviously results in an increase of the C activity in the matrix,<sup>23</sup> thus providing a composition gradient driving force for C diffusion towards the specimen center. The mechanism as to why the higher C activity in the subsurface regions results in C back diffusion rather than in decarburization in this case is discussed elsewhere.<sup>48</sup>

The back diffusion of C occurring during air oxidation of alloy 230 is not related to a composition gradient, as frequently described for cases in which Cr depletion results in dissolution of Cr-rich

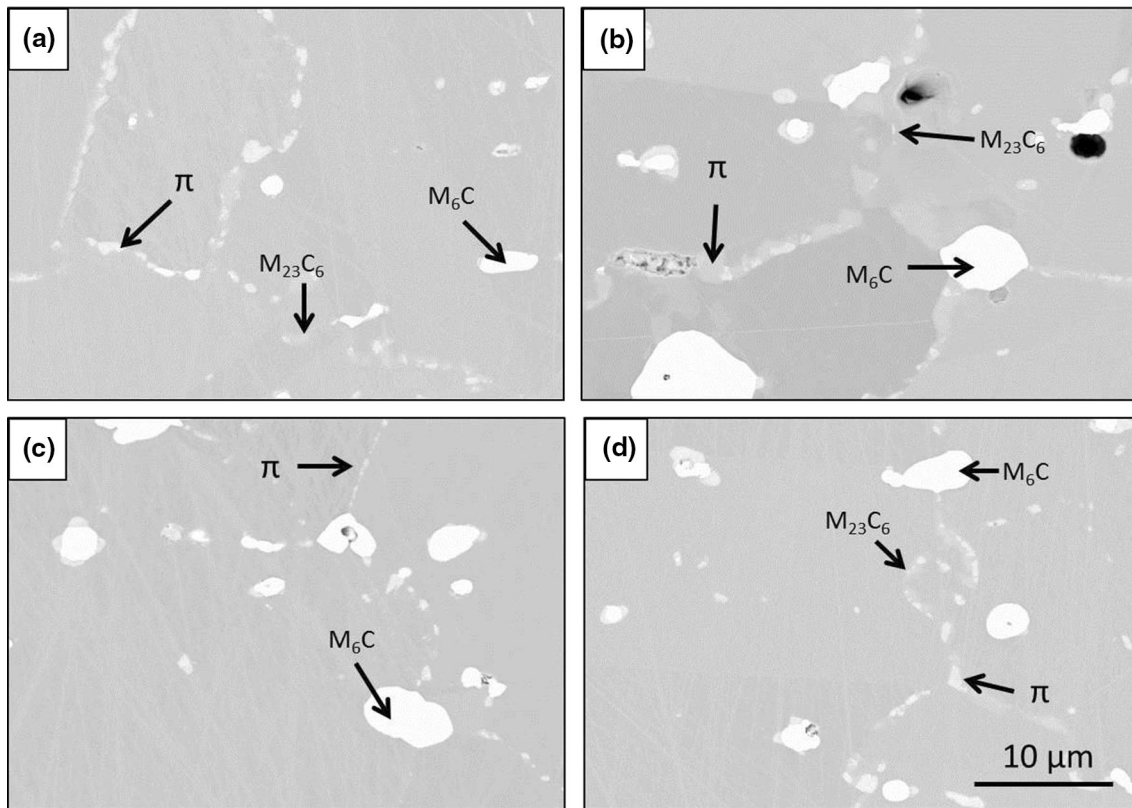


Fig. 9. BSE images for (a, b) 0.2-mm and (c, d) 0.5-mm-thick alloy 230 specimens after reaction for (a, c) 1000 h and (b, d) 3000 h at 950°C in laboratory air.

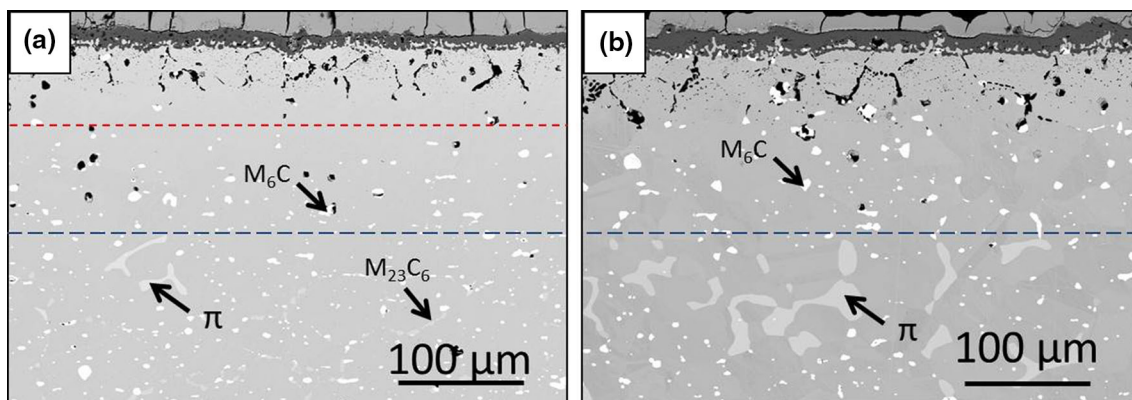


Fig. 10. BSE images of 0.5-mm-thick alloy 230 after reaction for (a) 1000 and (b) 3000 h at 1050°C in laboratory air (Blue and red dashed lines indicate the width of the zones free of  $M_6C$  and Cr-rich precipitates, respectively).

carbides.<sup>7</sup> Here, the back diffusion occurs due to an activity gradient driving diffusion. The increased C activity is mainly due to the effect of Cr loss on  $M_6C$  stability and the thermodynamic interaction among Cr, C and W in the  $\gamma$ -Ni-matrix.

Obtaining quantitative experimental confirmation of the C enrichment in the specimen center is not possible from EDX or WDX measurements, e.g., due to the multiphase character of the microstructure. A suitable method for measuring the total C content is GDOES. However, depth profiling by

sputtering through the surface scale and the relatively wide subscale depletion zone result in a very deep sputter crater. It is well established that the measurement accuracy may substantially decrease with increasing crater depth, because of crater side effects and non-flatness of the sputter crater. Therefore, a different approach was used to measure the C and N contents in the specimen center. Specimens of 0.5 mm thickness after exposure at 1000°C for 1000 h and 3000 h (compare microstructures in Fig. 7a and b) were carefully

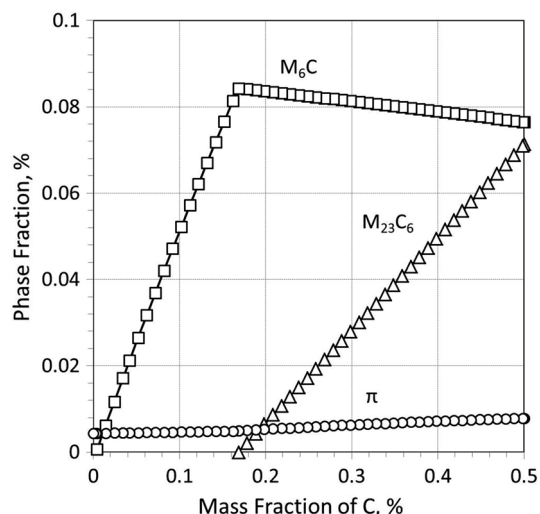


Fig. 11. Molar fractions of different phases in alloy 230 as a function of C content at 1000°C (calculated by Thermo-Calc using database TTNI7). For details: see text.

ground until reaching the center of the specimen. Due to the limited accuracy of the grinding method and the very limited width of the precipitate-containing zones (Fig. 7), this procedure was unfortunately not possible for the 0.3- and 0.2-mm specimens.

The ground surfaces, corresponding to the center of the 0.5-mm specimens, were analyzed by GDOES. For obtaining the relative sensitivity factors<sup>22</sup> for the various elements, a non-exposed alloy 230 specimen was analyzed using the same sputtering parameters as used for the two oxidized specimens, taking into account the known bulk alloy composition (Table I). The quantified depth profiles as a function of sputtering time for the specimen exposed for 3000 h in Fig. 14 shows that the average C content in the specimen center was 1.03 at.% (compared to 0.48 at.% present in the as-received material). For the 1000 h (results not shown here), the C content in the specimen center was 0.74 at.%. Figure 14 also indicates that, for the 3000 h specimen at a depth corresponding to a sputtering time of approximately 1300 s, the C content decreased, eventually reaching values which were even lower than the C content in the as-received material. The sputter time at which this effect occurs thus corresponds to the subscale carbide free zone shown in Fig. 7d. These results clearly illustrate that indeed a C back diffusion occurred as a result of the mechanisms described above. After the 3000 h exposure at 1000°C, this resulted in an approximate doubling of the C content in the center of the 0.5-mm specimen. As the C diffusivity is orders of magnitude larger than that of the carbide forming elements (here mainly Cr and W) and most of the C in the specimen center is tied up in form of carbides, the C concentrations are mainly governed by profiles of the mentioned metallic elements, i.e. they are relatively flat.

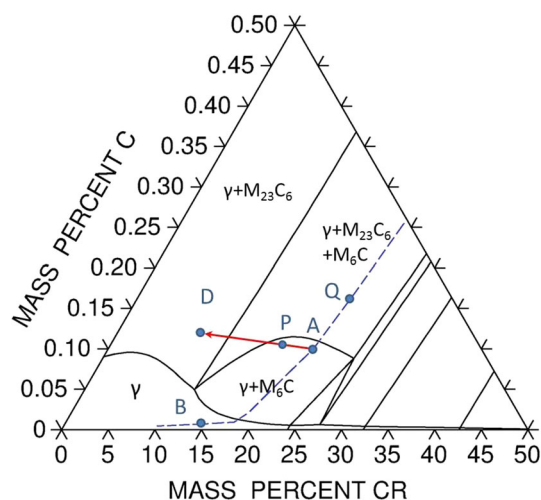


Fig. 12. Section of the Ni–Cr–W–Mo–C phase diagram at 1000°C for constant W and Mo contents of 14% and 2%, respectively, calculated in Thermo-Calc using the TTNI7 database. The dashed line indicates isoactivity for which the chemical potential (activity) of the C is constant.

Specimen or component thickness is an important consideration for the discussion of the oxidation-induced microstructural changes. In thin specimens, as studied here, the Cr reservoir was limited. In addition, the C diffusing from the surface will enrich the center. For a component several millimeters thick, the C released from the subsurface depletion zone will only make a minor change in the C content of the wide zone at the center of the component. For these thin specimens, the width of the subsurface depletion zone becomes similar or larger than the width of remaining carbide-containing zone after long times or at the highest temperatures, e.g. Fig. 7f. Even for the 0.5-mm specimen, the C content in the specimen center after a 3000 h exposure approximately doubled compared to that in the as-received material, as shown in Fig. 14. In Fig. 12, this increase in C content would correspond to movement on the isoactivity line to point Q. Once the C concentration exceeds 0.14 wt.%, Cr-rich  $M_{23}C_6$  becomes stable with a resulting decrease in the Cr concentration in the  $\gamma$ -Ni matrix. For simple geometrical reasons, it is apparent that the relative enrichment of C in the specimen center will tend to be even larger for the 0.3- and 0.2-mm specimens.

For the case in which the W-rich  $M_6C$  carbides completely dissolve in the 0.2-mm-thick specimen after 3000 h at 1000°C (Fig. 7f), the Cr profile showed significant Cr depletion across the entire specimen, such that the average Cr content in the specimen had dropped from 22 down to  $\sim$ 12 wt.% (Fig. 2b). In Fig. 12, that depletion corresponds to the red arrow path from point A to point D and a transition from the three-phase field  $\gamma$ -Ni +  $M_6C$  +  $M_{23}C_6$  region towards the two-phase field  $\gamma$ -Ni +  $M_{23}C_6$  region with no  $M_6C$  present. One assumption in Fig. 12 is that the concentration of W and Mo remain at the original levels of 14% and 2%, respectively. In reality,



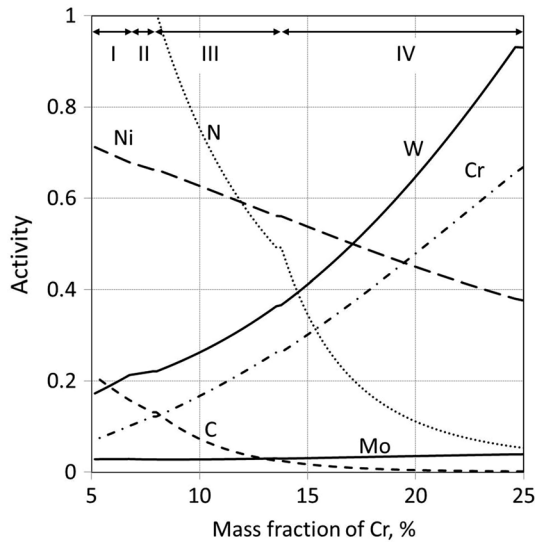


Fig. 13. Activities of different elements in alloy 230 as a function of Cr content at 1000°C, calculated by Thermo-Calc. Areas indicated I–IV relate to phase fields  $\gamma + M_{23}C_6$ ,  $\gamma + M_{23}C_6 + M_6C$ ,  $\gamma + M_6C + M(N,C)$  and  $\gamma + M_6C + \pi$ , respectively.

however, the Cr depletion may affect the activities of these elements (Fig. 15), thus establishing W and Mo activity gradients between the subscale depletion zones and the specimen center.

For developing a more detailed description of the mechanism of the  $M_6C/M_{23}C_6$  transformation discussed above, a set of calculations was performed in DICTRA to simulate the experimentally observed oxidation-induced phase transformations. Similar to the thermodynamic calculations, five elements were taken into account, i.e. Ni, Cr, W, Mo, and C. A time-dependent outward Cr flux, derived from the experimentally determined oxidation data, was set as a boundary condition to simulate the oxidation-induced Cr depletion, using the procedure described elsewhere.<sup>23</sup> Figure 15 shows the calculated and measured concentration profiles in a 0.3-mm-thick specimen after oxidation for 1000 h at 1000°C. Good agreement between the measured and calculated Cr profiles was obtained, which implies that the Cr depletion kinetics were accurate. However, the calculated W profile did not completely match with the experimental one in the near-surface region, although the W subsurface enrichment was qualitatively correct. The reason for the inaccuracy is the inability of DICTRA to take into account the interface displacement due to metal consumption by the scaling process. While this effect is virtually negligible for thick specimens, the moving boundary effect distorts the depletion calculations in a 0.3-mm-thick specimen. For a better quantitative description of the depletion kinetics, interface displacement has to be implemented into the model. However, commercial software packages like DICTRA do not so far provide this option. Modeling approaches developed to account for this effect have been described elsewhere,<sup>16,23</sup> but fall outside the scope of the present investigation.

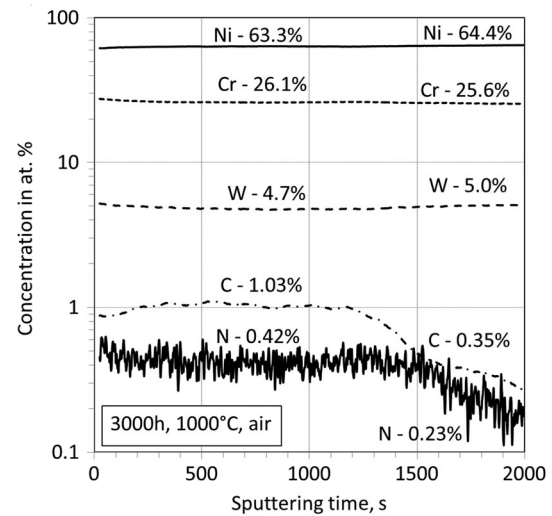


Fig. 14. Element concentrations as function of sputter time for 0.5-mm alloy 230 sample after 3000 h exposure at 1000°C. Before the GDOES measurement, the specimens was ground to half thickness. Thus, the left part of the diagram (sputter time equals 0 s) corresponds to the center of the specimen.

According to the thermodynamic calculations (see Fig. 11), the  $M_{23}C_6$  carbide is not stable in the as-received condition in alloy 230. Based on the above considerations, it forms in the specimen center after back diffusion has resulted in an overall C content higher than the critical value of 0.16 wt.%. The C migration from the Cr-depleted zone towards the specimen core is a dynamic process and it requires a certain time until the C enrichment in the center of the foil exceeds the threshold for  $M_{23}C_6$  formation, which is 0.14 wt.% at 1000°C, according to the calculated phase diagram (Fig. 12). For a given oxidation condition (i.e. the depth of the Cr-depleted zone), the critical C concentration required for carbide formation will be reached after shorter oxidation times in a thin than in a thick specimen. This is in agreement with the 950°C results presented in Fig. 9.

The DICTRA calculations in Fig. 16 thus at least qualitatively correctly describe (1) the formation of a  $M_6C$  depleted zone (2) the initially unstable Cr-rich  $M_{23}C_6$  carbide forms due to the subscale Cr depletion and the C back diffusion, and (3) the accompanied decrease in the  $M_6C$  volume fraction.

The total calculated decrease in volume fraction of  $M_6C$  was smaller than experimentally observed. This discrepancy is related to the formation of nitride along with oxidation Cr depletion in the specimen center, as will be illustrated in the following section.

### Modelling Nitride Formation in the Center of the Specimen

The high volume fractions of nitride in the (thin) specimen after long exposure time are indicative of nitridation. Apart from back diffusion of N similar to that of C, there was also substantial N ingress

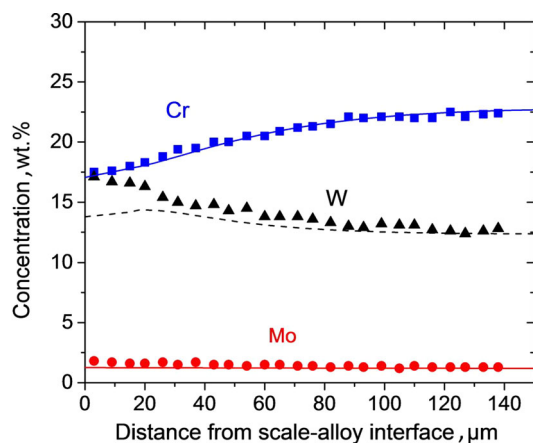


Fig. 15. Comparison of Cr, W and Mo concentration profiles in the  $\gamma$ -Ni matrix measured by EDX (symbols) in the studied 0.3-mm-thick specimen of alloy 230 with DICTRA calculations (lines) after 1000 h oxidation at 1000°C in laboratory air. Measured oxidation kinetics used as input for the calculation were taken from the gravimetric data in Fig. 1.

from the environment. In the current type of experiments involving oxide growth, oxide spallation and N uptake, it was virtually impossible to accurately estimate the nitridation kinetics and the incubation time (nitridation occurs after the occurrence of a certain Cr depletion). With so many experimental unknowns, diffusion calculations would be extremely inaccurate and inconclusive.

Therefore, another attempt was made to rationalize the experimentally observed microstructural changes, using phase equilibria calculated by ThermoCalc and the data base TTNI7. Based on the activity data in Fig. 13, the subscale Cr depletion would result in a back diffusion of N in a similar manner as described for C. This was confirmed by the GDOES results shown in Fig. 14. Although the measured concentrations for N were nearer to the detection limits (as indicated by the larger signal to noise ratio) than is the case for C, the results clearly revealed that an increase of the N content in the specimen center occurred whereby the N content increased with increasing exposure time. The database TTNI7 considers various types of nitride phases, i.e. mainly  $\text{Cr}_2\text{N}$ . The nitride phase present after a very short (100 h) exposure time (Fig. 3) could not, be unequivocally identified, as described in previous sections. The nitride in the specimen center, however, could clearly be correlated with  $\pi$ -phase (see Fig. 6b). The composition of this phase at 1000°C for the alloy 230 composition in the data base TTNI7 is 57Cr-36Ni-2Mo-5N (in wt.%). Compared to the actually measured nitride composition, e.g., in Fig. 4 (39Cr-32Ni-24W-4Mo in wt.%), the database TTNI7 did not take into account W solubility; however, Mo solubility was correctly described.

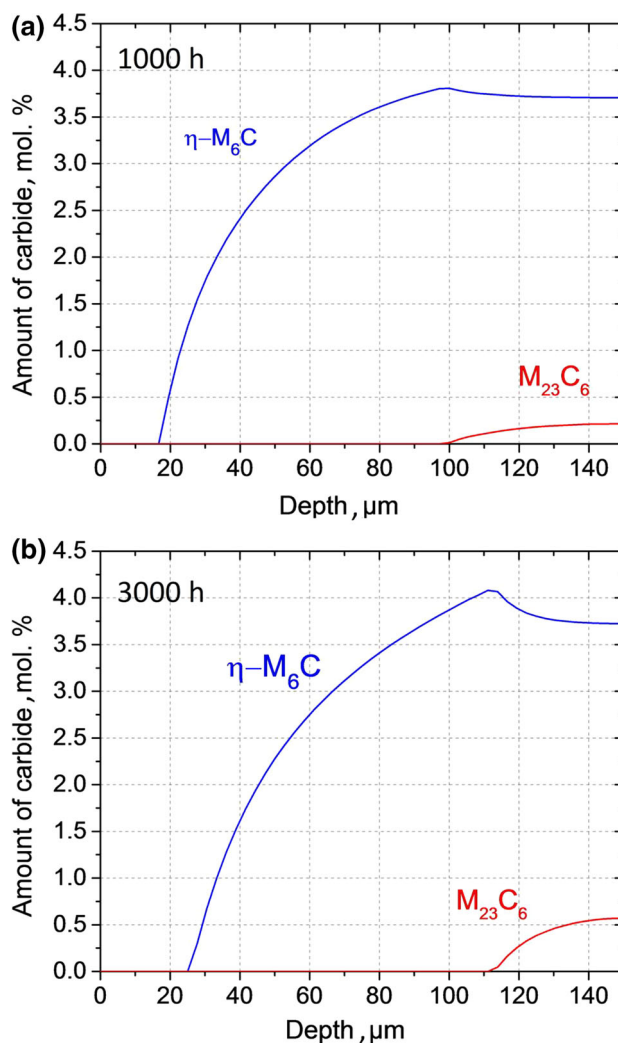


Fig. 16. DICTRA calculation profiles showing volume fractions of  $\text{M}_6\text{C}$  and  $\text{M}_{23}\text{C}_6$  in the 0.3-mm-thick specimen of alloy 230 after (a) 1000 h and (b) 3000 h at 1000°C in laboratory air. Input kinetics from Fig. 1, starting alloy composition from Table 1, and calculations in Fig. 11.

Considering that the  $\pi$ -phase is the only nitride formed, alloy 230 should at 1000°C exhibit a microstructure consisting of a  $\gamma$ -Ni matrix, W-rich  $\text{M}_6\text{C}$  and very minor amounts of  $\pi$ -phase (Fig. 11). A doubling of the C content and N content (see Fig. 14) by back diffusion resulted in the formation of a four-phase microstructure consisting of a  $\gamma$ -Ni matrix, W-rich  $\text{M}_6\text{C}$ , Cr-rich  $\text{M}_{23}\text{C}_6$  and  $\pi$ -phase (Fig. 17a).

Considering the densities of the mentioned phases ( $9 \text{ g cm}^{-3}$  for  $\gamma$ -Ni,<sup>49</sup>  $14.2 \text{ g cm}^{-3}$  for  $\text{M}_6\text{C}$ <sup>50</sup> and  $6 \text{ g cm}^{-3}$  for  $\pi$ -phase<sup>51</sup>) reveals that the volume fraction of  $\text{M}_6\text{C}$  in the alloy not affected by oxidation-induced depletion processes is approximately 2.7 vol.% whereas the volume fraction of  $\pi$ -phase is extremely small. If one assumes that the back diffusion of N would in the 0.3- and 0.2-mm specimens

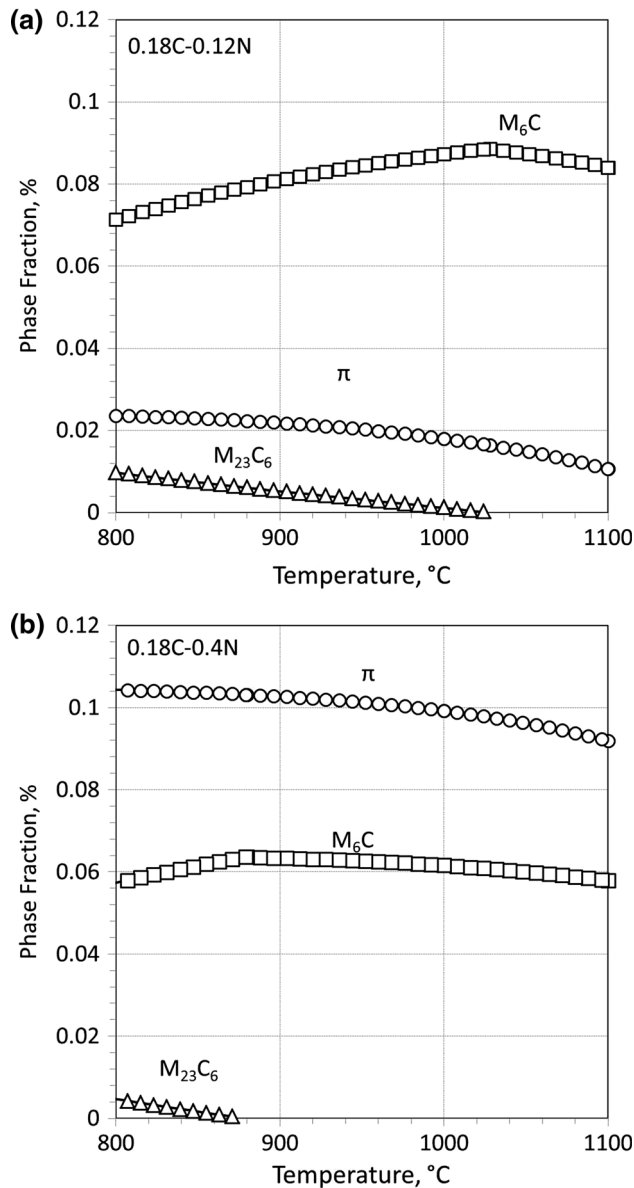


Fig. 17. Phase fractions in alloy 230 as function of temperature for various C and N contents. For details, see text.

result in a N content of 0.18 wt.%, i.e. even higher than found for the 0.5-mm specimen after 3000 h (Fig. 14), the volume fraction of the  $\pi$ -phase would be 3.9%. This is substantially lower than that experimentally observed for the thinnest specimens after 3000 h at 1000°C (Table III). This leads to the conclusion that, upon increasing exposure time and decreasing specimen thickness, the high volume fractions of nitride in the specimen center was not only related to back diffusion of N but additionally to uptake of N from the atmosphere (Fig. 17b). This is probably related to the fact that the substantial decrease in Cr interface concentration substantially lower than  $\sim 15\%$  which occurred during long-term exposure (Fig. 2) resulted in a loss of protective

properties of the surface oxide scale, which then may become prone to transport of gas molecules such as N.

Assuming a doubling of C content (due to back diffusion) and an even greater than doubling of the N content in the specimen core, the resulting phase fractions are shown in Fig. 14. Here, the C content was set at twice the original value and the N content arbitrarily to a high value of 0.4%, i.e. substantially higher than twice the original value used in Fig. 14. This resulted in a substantial increase in the phase fraction of  $\pi$ -phase and, at 1000°C, a slight decrease in phase fraction of  $M_6C$  and a vanishing of the  $M_{23}C_6$ , which is in agreement with the experimental observations (Fig. 7e and f). The dissolution of the Cr-rich carbide will obviously result in an increase of the C activity in the center of the specimen. This is expected to result in a redistribution of C in the specimen. This may be the qualitative explanation for the observations illustrated in Fig. 10 where after 1000 h a subscale  $M_6C$ -free zone was clearly found, whereas after 3000 h this was not the case.

The thermodynamic calculations in Fig. 17b do not predict that the formation of large volume fractions of Cr-rich nitrides after long periods in the thinnest specimens is accompanied by the experimentally observed vanishing of  $M_6C$  (Figs. 7f and 8b). The effect occurs when the overall Cr content in the specimen core starts to decrease (Fig. 2). The thermodynamic calculations in Fig. 12 predict a decreasing volume fraction of  $M_6C$  upon substantially decreased Cr content; however, a complete vanishing of the  $M_6C$  was quantitatively not correctly described. The discrepancy might be related to the fact that the  $\pi$ -phase in the database TTNI7 does not consider W solubility. This is contrary to the experimentally observed composition in which, typically, 24 wt.% W was present in the  $\pi$ -phase. Due to this high W solubility, formation of the  $\pi$ -phase is expected to substantially decrease the W content in the  $\gamma$ -matrix which obviously should have a destabilizing effect on the Ni/W-rich  $M_6C$  phase. The vanishing of the  $M_6C$  phase (Figs. 7f and 8b) in the specimen core is thus likely caused by a combination of the substantial oxidation-induced Cr loss and the consumption of W by formation of the W-containing nitride.

## SUMMARY AND CONCLUSION

Thin (0.2–0.5 mm) specimens of alloy 230 oxidized at 950–1050°C in laboratory air for 1000–3000 h exhibited a microstructure which consisted of a  $\gamma$ -Ni matrix, Ni/W-rich  $M_6C$  and Cr-rich precipitates ( $M_{23}C_6$  and Cr-nitrides). The Cr loss due to oxidation resulted in a Cr-depleted subsurface zone in which the Cr-rich precipitates dissolved. In addition, the Cr-lean  $M_6C$  was also depleted in this zone. The width of the  $M_6C$ -free zone was always smaller than that of the zone which was free of Cr-rich precipitates (carbides and/or nitrides). In the center of the



specimens, Cr-rich  $M_{23}C_6$  and  $\pi$ -nitrides were formed. These effects increased with oxidation time and temperature and decreasing specimen thickness. Using thermodynamic and kinetic modeling, a mechanism was developed to explain these observations wherein the Cr depletion in the subsurface zone increased the local C and N activity, resulting in an activity gradient that drove back C and N to the center of the specimen. Because the specimens were thin, the relative change in C and N content is sufficient to stabilize the Cr-rich carbide ( $M_{23}C_6$ ) and nitride ( $\pi$ -phase) near the specimen center. DICTRA calculations using the measured oxidation kinetics as input data successfully predicted the measured Cr depletion profile and qualitatively predicted the other microstructural changes. With increasing exposure time and decreasing specimen thickness, precipitate formation in the specimen center gradually became affected by N uptake from the environment. This process resulted in enhanced nitride formation at the expense of the Cr-rich carbides, in qualitative agreement with the thermodynamic calculations. Ongoing Cr depletion additionally resulted in dissolution of the  $M_6C$  precipitates.

#### ACKNOWLEDGEMENTS

The authors would like to acknowledge Dr. K. Ohla from Haynes International for supplying the material. The authors would also like to acknowledge the Bundesministerium für Bildung und Forschung (BMBF) for funding part of this work under Grant No. 03EK3032. Assistance with ICP-OES analysis provided by H. Lippert and V. Nischwitz from the Central Institute for Engineering, Electronics and Analytics, ZEA-3, Forschungszentrum Jülich GmbH is greatly appreciated. The authors are grateful to the following colleagues in the Institute of Energy and Climate Research of the Forschungszentrum Jülich GmbH IEK-2 for assistance in the experimental work: R. Mahnke, H. Cosler, and A. Kick for the oxidation experiments, V. Gutzeit and J. Bartsch for metallographic studies, Dr. E. Wessel for EBSD investigations and Dr. Nowak for GDOES analyses. At ORNL, G. Garner, T. Lowe and T. Jordan assisted with the experimental work and the research was sponsored by the U.S. Department of Energy, U.S. Assistant Secretary for Energy Efficiency and Renewable Energy, Advanced Manufacturing Office (Combined Heat and Power Program).

#### REFERENCES

1. D.J. Young, *High Temperature Oxidation and Corrosion of Metals* (Oxford: Elsevier, 2008), p. 196.
2. A.V. Dean and P.J. Ennis, *Nucl. Technol.* 66, 117 (1984).
3. W.R. Johnson, L.D. Thompson, and T.A. Lechtenberg, *Nucl. Technol.* 66, 88–101 (1984).
4. R.H. Cook, *Nucl. Technol.* 66, 283 (1984).
5. H.M. Tawancy, *J. Mater. Sci.* 27, 6481 (1992).
6. D.L. Klarstrom and G.Y. Lai, *Proceedings 6th International Symposium on Superalloys* (Seven Springs, PA, Sept. 18–22, 1988).
7. P.J. Ennis, W.J. Quadackers, and H. Schuster, *Mater. Sci. Technol.* 8, 78 (1992).
8. U. Bruch, D. Schuhmacher, P.J. Ennis, and E. te Heesen, *Nucl. Technol.* 66, 357 (1984).
9. N. Birks, G.H. Meier, and F.S. Pettit, *Introduction to the High-Temperature Oxidation of Metals* (Cambridge: Cambridge University Press, 2006), p. 101.
10. R. Bauer, M. Baccalaro, L.P.H. Jeurgens, M. Pohl, and E.J. Mittemeijer, *Oxid. Met.* 69, 265 (2008).
11. H.E. Evans and A.T. Donaldson, *Oxid. Met.* 50, 457 (1998).
12. D.P. Whittle, D.J. Evans, D.B. Scully, and G.C. Wood, *Acta Metall.* 15, 1421 (1967).
13. H. Ackermann, G. Teneva-Kosseva, H. Koehne, K. Lucka, S. Richter, and J. Mayer, *Mater. Corros.* 59, 380 (2008).
14. U. Brill, *Metallurgy* 46, 778 (1992).
15. U. Brill and J. Klöwer, *Metallurgy* 51, 263 (1997).
16. R. Pillai, H. Ackermann, H. Hattendorf, and S. Richter, *Corros. Sci.* 75, 28 (2013).
17. R. Pillai, H. Ackermann, and K. Lucka, *Corros. Sci.* 69, 181 (2013).
18. R.N. Durham, B. Gleeson, and D.J. Young, *Oxid. Met.* 50, 139 (1998).
19. P.J. Maziasz, B.A. Pint, J.P. Shingledecker, N.D. Evans, Y. Yamamoto, K.L. More, and E. Lara-Curzio, *Int. J. Hydrogen Energy* 32, 3622 (2007).
20. R. Duan, A. Jalowicka, P. Huczowski, B. Pint and W.J. Quadackers, Forschungszentrum Juelich GmbH, unpublished research (2015).
21. B.A. Pint, P.T. Tortorelli, and I.G. Wright, *Oxid. Met.* 58, 73 (2002).
22. W.J. Quadackers, A. Elschner, W. Speier, and H. Nickel, *Appl. Surf. Sci.* 52, 271 (1991).
23. A. Chyrkin, R. Pillai, H. Ackermann, H. Hattendorf, S. Richter, W. Nowak, D. Grüner, and W.J. Quadackers, *Corros. Sci.* 96, 32 (2015).
24. “High Temperature Tech Brief” Haynes International, 2009, <http://www.haynesintl.com/pdf/h3060.pdf>. Accessed 16 July 2015.
25. B.D. Bastow, D.P. Whittle, and G.C. Wood, *Oxid. Met.* 12, 413–438 (1978).
26. D. Klarstrom, *Corrosion*, 407/1-407/12 (1994).
27. L. Jiang, R. Hu, H. Kou, J. Li, G. Bai, and H. Fu, *Mater. Sci. Eng. A* 536, 37 (2012).
28. P. Subramanya Herle, M.S. Hegde, K. Sooryanarayana, T.N. Guru Row, and G.N. Subbanna, *J. Mater. Chem.* 8, 1435 (1998).
29. V. Gavriljuk and H. Berns, *High Nitrogen Steels, Structure, Properties, Manufacture, Applications* (Berlin: Springer, 1999).
30. C.S. Giggins and F.S. Pettit, *J. Electrochem. Soc.* 118, 1782 (1971).
31. C.S. Tedmon, *J. Electrochem. Soc.* 113, 766 (1966).
32. H.C. Graham and H.H. Davis, *J. Am. Ceram. Soc.* 54, 89 (1971).
33. D. Young and B. Pint, *Oxid. Met.* 66, 137 (2006).
34. M. Michalik, M. Hänsel, J. Zurek, L. Singheiser, and W.J. Quadackers, *Mater. High Temp.* 22, 213 (2005).
35. D. Kim, C. Jang, and W.S. Ryu, *Oxid. Met.* 71, 271 (2009).
36. W.J. Quadackers, J. Piron-Abellan, V. Shemet, and L. Singheiser, *Mater. High Temp.* 20, 115 (2003).
37. “MNX - MEMS and Nanotechnology Exchange” <https://www.memsnet.org/material/chromiumoxidecr2o3bulk/?keywords=chromium%20oxide>. Accessed 08 July 2015.
38. H. Evans, *Int. Mater. Rev.* 40, 1 (1995).
39. W.J. Quadackers, P. Huczowski, D. Naumenko, J. Zurek, G.H. Meier, L. Niewolak, and L. Singheiser, *Mater. Sci. Forum* 595–598, 1111 (2008).
40. J. Zurek, G.H. Meier, E. Essuman, M. Hänsel, L. Singheiser, and W.J. Quadackers, *J. Alloys Compd.* 467, 450 (2009).
41. W.J. Quadackers and L. Singheiser, *Mater. Sci. Forum* 369, 77 (2001).
42. S. Osgerby, K. Berriche-Bouhanek, and H.E. Evans, *Mater. Sci. Eng. A* 412, 182 (2005).
43. A. Baldan, *J. Mater. Sci.* 37, 2171–2202 (2002).

44. A. Chyrkin, P. Huczkowski, V. Shemet, L. Singheiser, and W.J. Quadackers, *Oxid. Met.* 75, 143 (2010).
45. K. Ledjeff, A. Rahmel, and M. Schorr, *Werkst. Korros.* 30, 767 (1979).
46. P. Berthod, C. Vebert, L. Aranda, R. Podor, and C. Rapin, *Oxid. Met.* 63, 57 (2005).
47. R. Petkovic-Luton and T.A. Ramanarayanan, *Oxid. Met.* 34, 381 (1990).
48. W.J. Quadackers, *Mat. Sci. Eng.* 87, 107 (1987).
49. "MNX - MEMS and Nanotechnology Exchange" <http://www.memsnet.org/material/nickelnibulk/?keywords=nickel>. Accessed 08 July 2015.
50. P. Villars, "Material Phases Data System (MPDS)" (Springer-Verlag GmbH, Heidelberg, 2014) [http://materials.springer.com/isp/crystallographic/docs/sd\\_0540673](http://materials.springer.com/isp/crystallographic/docs/sd_0540673). Accessed 09 July 2015.
51. P. Villars, "Material Phases Data System (MPDS)" (Springer-Verlag GmbH, Heidelberg, 2014) [http://materials.springer.com/isp/crystallographic/docs/sd\\_1008647](http://materials.springer.com/isp/crystallographic/docs/sd_1008647). Accessed 09 07 2015.